Accepted Manuscript

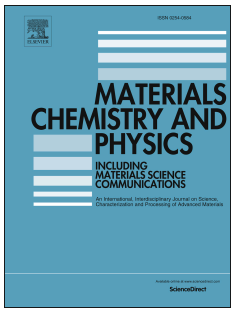

Effect of different functionalized carbon nanostructures as fillers on the physical properties of biocompatible poly(L-lactic acid) composites

Nicola Vicentini, Teresa Gatti, Marco Salerno, Yuriko Suemi Hernandez Gomez, Mattia Bellon, Sasha Gallio, Carla Marega, Francesco Filippini, Enzo Menna

PII: S0254-0584(18)30304-3

DOI: 10.1016/j.matchemphys.2018.04.042

Reference: MAC 20537

To appear in: *Materials Chemistry and Physics*

Received Date: 23 January 2018

Revised Date: 9 March 2018

Accepted Date: 9 April 2018

Please cite this article as: N. Vicentini, T. Gatti, M. Salerno, Y.S. Hernandez Gomez, M. Bellon, S. Gallio, C. Marega, F. Filippini, E. Menna, Effect of different functionalized carbon nanostructures as fillers on the physical properties of biocompatible poly(L-lactic acid) composites, *Materials Chemistry and Physics* (2018), doi: 10.1016/j.matchemphys.2018.04.042.

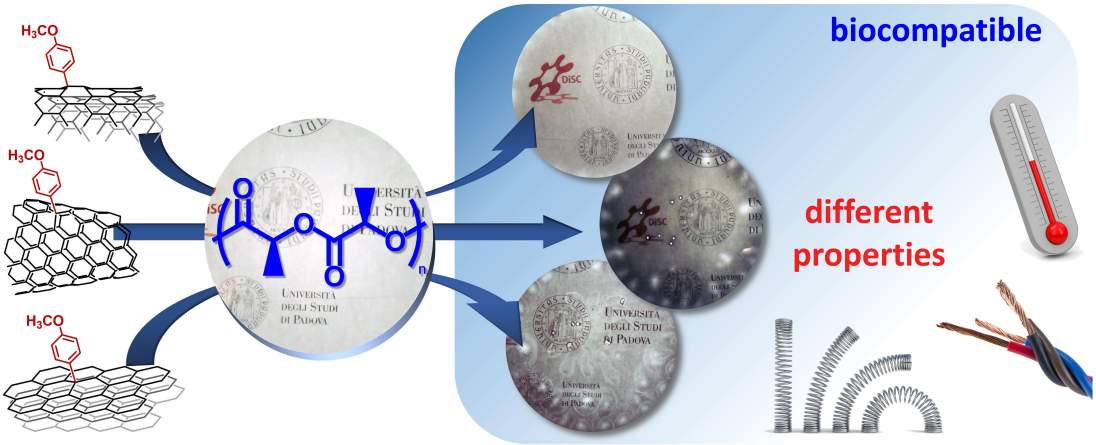

Effect of different functionalized carbon nanostructures as fillers on the physical properties of biocompatible poly(L-lactic acid) composites

Nicola Vicentini,[a] Teresa Gatti,[a,*] Marco Salerno,[b] Yuriko Suemi Hernandez Gomez,[c] Mattia Bellon,[c] Sasha Gallio,[a] Carla Marega,[a] Francesco Filippini,[c] Enzo Menna[a,d,*]

[a] Department of Chemical Sciences, University of Padova and INSTM UdR Padova, Via Marzolo 1, 35131 Padova, Italy

[b] Materials Characterization Facility, Istituto Italiano di Tecnologia, Via Morego 30, 16163 Genova, Italy

[c] Department of Biology, University of Padova, Via Bassi 58/B, 35131 Padova, Italy

[d] Centre for Mechanics of Biological Materials, University of Padova, Via Marzolo 9, 35131 Padua, Italy

[*] Corresponding authors: teresa.gatti@unipd.it; enzo.menna@unipd.it

Abstract

Composites of carbon nanostructures (CNSs) and biocompatible polymers are promising materials for a series of advanced technological applications, ranging from biomedicine and bioelectronics to smart packaging and soft robotics. In this work, we present three types of organic-functionalized CNSs, namely *p*-methoxyphenyl functionalized multi-walled carbon nanotubes, carbon nanohorns and reduced graphene oxide, used as nanofillers for the preparation of homogeneous and well-dispersed composites of poly(L-lactic acid), a biocompatible and biodegradable FDA-approved polymer. A thorough characterization of the composites is given in terms of calorimetric response, electrical and mechanical properties. Significant differences are observed among the different types of CNS nanofillers, underlying the key role played by the nanoscale shape and distribution of the components in driving the macroscopic behavior of the composite material. Surface properties are probed through advanced atomic force microscopy techniques, on both flat substrates (films) and confined systems (nanofibers). All these composites proved to be biocompatible and to support as scaffolds the proliferation of human neuronal precursor cell line SH-SY5Y, opening the route to a future comparative analysis on their ability to boost neuronal differentiation.

Keywords

Nano composites, Carbon nanostructures, Biocompatibility, Electrical properties, Mechanical properties, Thermal properties, Electro-spinning

1. Introduction

Carbon nanostructures (CNSs), including carbon nanotubes (CNTs) and graphene-based materials (GBMs), are largely employed fillers for polymer phases, being able to confer novel properties to

these last ones, such as improved electrical/thermal conductivities and mechanical reinforcement [1-5].

Among polymeric materials, biocompatible and biodegradable polymers [6] are of great interest for the scientific and industrial community due to their intrinsic sustainability, being derived from renewable sources and being suitable for recycling and/or biodegradation.

Composites of CNSs and biocompatible polymers can combine the properties of the two constituents and act as functional materials for a number of technological applications,[7, 8] which include medical devices and implants [9-12], tissue engineering [13-24], drug delivery [25, 26], bio-, green and wearable electronics [27-29], biosensing [29-34], soft robotics [35, 36] and smart packaging [37-39].

When attempting to combine biocompatible polymers with CNSs with the aim of fabricating a good quality composite, one has to face major obstacles related to the often profound physical incompatibility between the two materials. In fact, while the polymer is more hydrophilic, pristine CNSs are hydrophobic and in addition have a pronounced tendency to aggregate, because of the strong van der Waals interactions between π-electron clouds. High-power ultrasonication and/or shear mixing can sometimes help in blending the two components [40], however these processes are not always effective, and harsher conditions can induce deterioration of the CNSs [41-43]. As alternative approaches, current chemical strategies aim to increase the affinity between the two phases by either adding surfactants [44] or chemically functionalizing the external surface of CNSs with suitable organic groups [8, 45-47]. This latter option, particularly suitable for high added-value applications, has the advantage of being tunable with respect to the type and amount of organic moieties inserted onto the CNSs, making it possible to direct the properties of the final material [48]. In this case, the primary goal is an improved compatibility and homogeneous dispersion in an environment having a given polarity, either a solvent or a polymer matrix. We have recently demonstrated the effectiveness of this strategy, by functionalizing multi-walled CNTs (MWCNTs) with *p*-methoxyphenyl groups through a diazotization process, involving the *in situ* generation of aryl radical reactive species starting from the corresponding aniline derivative [49]. By tuning reactant amounts and reaction times, solubility of the functionalized species can be directed towards different solvent polarities.

In addition, we have shown that *p*-methoxyphenyl functionalized MWCNTs (MWCNT-PhOMe) can be efficiently dispersed in poly(l-lactic acid) (PLLA), - a FDA-approved biocompatible and biodegradable polymer - and the resulting composites (MWCNT-PhOMe@PLLA) can be processed in the form of free-standing homogeneous films [13] and electrospun nanofibers [14] able to

promote neuronal growth and differentiation starting from either SH-SY5Y human neuroblastoma cells [13, 14] or human circulating multipotent stem cells from peripheral blood [15].

Different dimensionalities of CNSs such as CNTs, reduced graphene oxide (RGO) and carbon nanohorns (CNHs) give rise to different properties and may induce different behaviors on composite materials when used as fillers [50-52]. A comparison of the physical properties of the resulting composites could help tailoring novel materials for specific applications and, when considering cell growth scaffolds, hints could be gained about physical properties' influence on cellular processes. We report in the present work novel types of functionalized-CNS@PLLA composites based on different CNSs, namely *p*-methoxyphenyl decorated RGO [53] (RGO-PhOMe) and *p*-methoxyphenyl decorated CNHs (CNH-PhOMe), synthesized analogously to MWCNT-PhOMe. We also consider more MWCNT-PhOMe@PLLA composites, by testing the effect of increasing CNT contents in PLLA. A detailed overview of the macroscopic properties of these composite materials is provided, involving electrical, mechanical and thermal characterizations as a function of the type and concentration of nanofillers. Surface properties are probed through advanced atomic force microscopy (AFM) techniques on both flat and nanoscale confined systems (single composite nanofibers). Finally, proofs of their biocompatibility with neuronal precursors are given, opening the route to future experiments testing their ability to favor neuronal differentiation.

2. Experimental

2.1 Materials

All reagents and solvents were purchased from Sigma-Aldrich and used as received if not otherwise specified. MWCNTs were produced by SouthWest NanoTechnologies with the CVD method and have the following dimensions: outer diameter 10 nm ± 1 nm, internal diameter 4.5 nm ± 0.5 nm, lengths 3-6 μm. CNHs were purchased from Carbonium s.r.l. (Padua, Italy) and present a dahlia-type shape with a diameter of 60-120 nm. RGO powder was purchased from ACS Material, LLC (product No.: GnP1L-0.5g). The RGO production method, as reported by the supplier, consists in completely reducing graphene oxide obtained via the Hummer's method through thermal exfoliation reduction and further hydrogen reduction. Reduced graphene oxide flakes have lateral dimensions between 1 and 2 μm, are constituted of few layers overlapping irregularly and have many corrugations (see refs. [53-56]).

2.2 Synthesis of *p*-methoxyphenyl functionalized CNSs

Functionalization of MWCNTs, CNHs and RGO was carried out following the previously reported diazotization procedure (Scheme S1), with slight modifications [14, 53]. For each CNS, the stoichiometry of the reaction has been optimized in order to obtain the maximum gain in chloroform solubility. For the sake of clarity, details are given here.

A dispersion of as purchased CNSs (75 mg, 6.25 mmol of C) in 1-cyclohexyl-2-pyrrolidone (CHP) (35 mL), pre-sonicated for 10 min (power level: 2.0, pulse on: 3 s, pulse off: 3 s) was transferred to a two-necked round-bottomed flask. A solution of 4-methoxyaniline (385 mg, 3.13 mmol for the functionalization of MWCNTs and RGO; 770 mg, 6.25 mmol for the functionalization of CNHs) in 15 mL of CHP was added and the mixture was heated to 80 °C under a nitrogen atmosphere. Then, isopentylnitrite (0.42 mL, 3.12 mmol for the functionalization of MWCNTs and RGO; 0.84 mL 6.25 mmol for the functionalization of CNHs) was added carefully. After 15 min of continuous stirring, the reaction mixture was diluted with cold methanol (500 mL) and filtered on a PTFE membrane (Fluoropore 0.2 um). The filtrate was washed with methanol (4 x 200 mL) and dried under an IR lamp for 30 min. For each CNS the functionalization procedure was repeated 3 times in order to obtain the amount of *p*-methoxyphenyl functionalized CNSs required for the preparation of the composite materials.

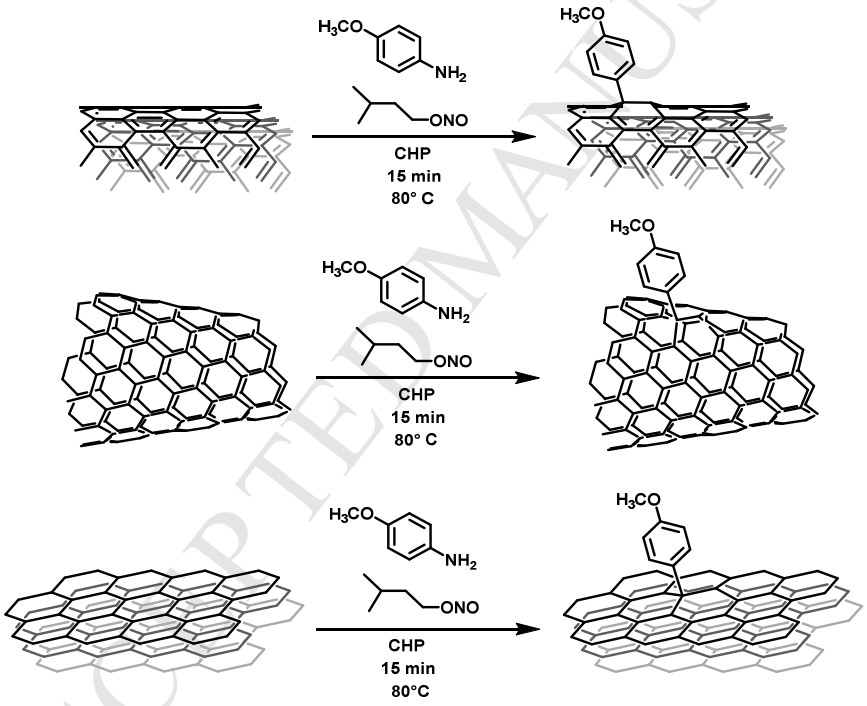

Scheme S1. Covalent functionalization of MWCNTs (top), CNHs (center) and RGO (bottom) with *p*-methoxyphenyl substituents via diazotization reactions.

2.3 Preparation of functionalized-CNS@PLLA films

p-methoxyphenyl-CNS@PLLA blend solutions in $CHCl_3$ were prepared by adding a dispersion of MWCNT-PhOMe or CNH-PhOMe or RGO-PhOMe in chloroform obtained through sonication (power level: 2.0, pulse on: 3 s, pulse off: 3 s, 5 min) to a chloroform solution of PLLA (6 wt%) under continuous stirring. The amount of *p*-methoxyphenyl-CNS within the various blends was varied among 0.1, 0.25, 0.5, 1 and 5 wt% with respect to the polymer content. Films of the various composite materials were obtained through solvent evaporation into a petri dish at 50 °C and each

of them had a diameter of 6 cm (see Fig. S4 in the Supplementary Information – S.I. - for pictures). For mechanical characterization, samples were cut into 5 identical specimens each with sizes of 40 mm x 10 mm x 0.3 mm. These are not standardized specimens, intended for internal comparison only, and the tensile data are not therefore comparable with literature data.

2.4 Characterization of functionalized-CNS@PLLA films

Absorbance values at 1000 nm were measured with a Varian Cary 5000 spectrophotometer. DSC measurements were carried out with a DSC Q20 (TA Instruments) under nitrogen by heating the samples at 1 °C min^{-1} over a temperature range from 40 to 200 °C. A complete heating-cooling-reheating cycle was carried out to eliminate thermal history of the samples, and thermograms from the second heating stage (reheating) are reported. The thickness of each sample was measured in different points using a Mitutoyo Digimatic micrometer with a precision of 10^{-4} cm. Tensile mechanical properties of rectangular-shaped specimens were measured using an Instron model 3300 mechanical tester at room temperature. The strain rate was 10 mm min^{-1}. At least five measurements were performed for each sample. The surface resistance of the films was measured with two different instruments depending on resistance. For films with resistance lower than 10^6 Ω a digital multimeter, Keithley 2000 provided with 4 probes positioned at a distance of 1 cm with respect to each other was used. Each film sample was measured at different points and average values are given. For films with resistance higher than 10^6 Ω a Keithley electrometers for Ultra-High Resistance *6517B*, implemented with a resistivity text fixture (Model 8009) for measuring surface resistivity was used. Measurements were performed alternating the polarity between 100 V and -100 V and acquiring each point for 60 s. Average values over 10 repetitions are reported.

2.5 Preparation of functionalized-CNS@PLLA electrospun nanofibers

Solutions of *p*-methoxyphenyl-CNSs / PLLA blends (5 wt%) to be used for electrospinning were prepared following the same procedure described for the preparation of the films but using a $CHCl_3$:DMF 9:1 (v/v) mixture as solvent. The small DMF portion in the solvent was introduced in order to increase the boiling point, i.e. to optimize conditions for electrospinning. Electrospinning was performed on a home-made apparatus with an applied voltage of 18 kV, tip to collector distance of 20 cm and by maintaining a solution flow rate of 0.03 mL min^{-1} on the syringe pump injector. Transmission electron microscopy (TEM) images were recorded on samples spun directly onto TEM copper grids for 60 seconds with a Tecnai G2 microscope (FEI) operating at 100 kV. AFM images were recorded on samples spun onto Graphene Supermarket silicon prime wafers (oxide thickness: 285 nm) for 60 seconds (see AFM details later in the text).

2.6 Sample preparation for AFM

For the film samples, small specimens (~5 × 5 mm) were cut and mounted each on a different optical microscope glass slide (1" × 3") by means of double-sided sticky tape. In case of topographic-only measurements a standard tape was used, while for the CAFM measurements a conductive carbon tape (normally used for scanning electron microscopy as a drain layer for the injected electron beam current) was employed. The goal was to obtain a measurement of local transversal (i.e. out of plane) conductivity, perpendicularly to the film and through that, like the case of macroscopic measurements of film conductance. For the fiber samples, few fibers were directly deposited by electrospinning on an insulating substrate of oxidized silicon wafer. The fibers were sparse enough to allow us to address and image them independently. The fibers crossed the whole silicon substrate diameter and touched the substrate edges on both opposite sides. There, a contact was provided all around the substrate edges by means of silver paste. The goal was to obtain a measurement of local longitudinal (i.e. in plane) conductivity, axial to the fibers, and provide a value of single fiber conductivity. Because the fibers were contacted on both opposite side ends, and in order to minimize the possible voltage drop along the fiber, the measurements were always carried out on fiber regions close to one edge of the silicon substrate, in the range of 100-300 µm distance from that. In both cases of CAFM samples (films on carbon pad or fibers with silver paint) the contact was taken away to the AFM head by means of adhesive copper tape stuck to the glass slide, and, later on, at a magnetic contact pad, to the head through a thin compliant wire.

2.7 AFM measurements

All the AFM images were 256 × 256 pixels and were acquired on an MFP-3D instrument (Asylum Research, US) in ambient air. For the conductive AFM (CAFM) measurements, a probe of type AC240TM-R3 (Olympus, Japan) was employed, with cantilever resonance frequency of 66.62 kHz and spring constant of 1.81 N/m. The tip had a Ti/Pt coating of ~20 nm thickness, and thus an effective apex diameter of ~60 nm. Further technical details about the CAFM measurements are reported in the S.I., for the sake of space. For SKPM a probe of type PPP-EFM (Nanosensors, Switzerland) was used, with resonance frequency of 95.90 kHz. The tip has a Ti/PtIr5 coating of ~25 nm thickness, and thus an effective apex diameter of ~70 nm. The AFM was operated in lift (Nap) mode, with Tapping tracking of the topography during the first pass, and at an elevation of 100 nm during the second pass. During the latter pass, a feedback was applied on the tip voltage, a sum of AC and DC components, such that the electrical force between tip and sample (set at virtual ground) was canceled out. In some cases, to provide better understanding of the electrical surface properties, the analysis was switched from SKPM to qualitative EFM mode. While this is also based on two-pass technique, during the second pass the cantilever is dithered mechanically and the open-loop changes in oscillation phase are observed. On average, lower local phase lags of the

oscillating cantilever should correspond to net repulsive forces, while higher local phase lags should correspond to attractive forces. For the roughness measurements, Tapping mode AFM was carried out with a probe of type SSS-NCHR (Nanosensors, Switzerland), with cantilever resonance frequency of ~312.53 kHz. The most important amplitude parameter of surface roughness, namely 2-D root mean square (RMS) S_q has been extracted from the height distributions in the images, and averaged over all the images ($N \geq 5$).

2.8 Biological methods for the assessment of biocompatibility of the functionalized-CNS@PLLA scaffolds

Exponential growing human neuroblastoma SH-SY5Y cells[57] were cultured with Dulbecco's Modified Eagle Medium/Nutrient Mixture F-12 (DMEM/F-12) GlutaMAX™ supplement (Invitrogen) supplemented with 10% heat-inactivated fetal bovine serum (FBS, Euroclone) and 25μg/ml of gentamicin (growth medium), in a humidified atmosphere of 5% of CO_2 in air at 37 °C. Cells were subcultured - 900000 into 25 cm² flasks (Sarstedt) - every 2 days (i.e. at 90% confluence approximately). In control, scaffold-free samples, cells were seeded in a 24-well plate (15000 cells/well) coated with a gelatin (porcine skin 0.005% in H_2O milliQ)/poly-L-lysine (Invitrogen, 1mg/ml) solution. Poly-L-lysine is widely used as a good substrate for neural cell adhesion and growth. PLLA and CNS@PLLA films were cut into round slices with 13 mm diameter for well positioning into 24-well plates. After sterilization by UV irradiation, the films were incubated for 24h in growth medium and then cells (15000/well) were seeded onto their surfaces. Cell death and proliferation were assessed at day 0 (24 h after cell seeding) and day 2 (72 h after cell seeding) as reported in the S.I..

3. Results and discussion

3.1 Preparation of functionalized-CNS@PLLA composites

The three types of CNSs considered in this work, namely MWCNTs, RGO and CNHs, were first subjected to the functionalization process to obtain the corresponding *p*-methoxyphenyl derivatives. The functionalization reaction was carried out in cyclohexyl pyrrolidone (CHP) in the presence of *p*-methoxyaniline and isoamyl nitrite (see Scheme S1 and experimental details in section 2), as reported for both MWCNTs [14, 49], RGO [53] and CNHs (for the first time here). This direct arylation reaction (Tour-type reaction [58]) is a convenient procedure to obtain functionalized-CNSs with improved solubility profiles and diminished tendency to self-aggregation. In relatively short times (15 min in the present case) and in a single step, it is possible to obtain covalently decorated CNSs for the desired purpose. The choice to employ the same reaction and the same type of functional groups for all three selected CNSs is based on the need for comparing properties of the

nanomaterials *per se* and of the final PLLA composites containing them. Reactants amounts were screened in order to determine the best condition for achieving the highest dispersion of the functionalized CNSs in chloroform (the solvent of choice for PLLA). Particularly, the maximum dispersion of MWCNTs and RGO in chloroform was obtained when the reaction was carried out with 0.5 equivalents of *p*-methoxyaniline and isoamyl nitrite as compared to the moles of carbon contained in the CNSs, whereas for CNHs this happened when using one equivalent of reactants. The need for different amounts of reactants to gain the best solubility appears reasonable when considering the huge differences in nanomorphology existing among the three CNSs, which leads to different reactivity and tendency to aggregate. The resulting functionalized CNSs, namely MWCNT-PhOMe, RGO-PhOMe and CNH-PhOMe were characterized in terms of functionalization degree (FD), already used in previous works [49, 53, 54], which was determined with a good precision through thermogravimetric analysis (TGA; the corresponding thermograms are reported in Fig. S1, S2 and S3 in the S.I., together with an explanation of how FDs were calculated). Particularly FD values of 1/118, 1/47 and 1/44 were found for MWCNT-PhOMe, RGO-PhOMe and CNH-PhOMe, respectively, indicating that one *p*-methoxyphenyl substituent is present every 118, 47 and 44 carbon atoms of the CNS (the highest number obtained for MWCNT-PhOMe is consistent when considering that only carbons of the outer walls are reactive). The obtained CNS derivatives were effectively dispersed in chloroform and then mixed with PLLA in different weight percentages (wt%) with respect to the polymer, following the procedure described in the Experimental Section. In this way films of MWCNT-PhOMe@PLLA, RGO-PhOMe@PLLA and CNH-PhOMe@PLLA were prepared containing 0, 0.1, 0.25, 0.5, 1 and 5 wt% of functionalized CNSs in PLLA. The resulting films were all free-standing and characterized by a glossy texture (see Fig. S4 in the S.I.). Resulting thicknesses were uniform among the films and all included in the range between 300 and 350 μm (see Table S1 for the exact values). The good dispersion of the functionalized CNSs within the polymer matrix was evident after backlight inspection of the films with the lower concentrations of CNSs (0.1 wt%, see Fig. 1a), in which the presence of macroscopic aggregates was not evident, while at higher concentrations transparency was lost and backlight inspection was not feasible. Furthermore, it is worthy to state here that attempts to prepare composite films with pristine-CNSs and PLLA at 0.25 wt% (a relatively low nanofiller concentration) following the same procedures, resulted in the formation of highly un-homogeneous materials, presenting internal fractures and CNS aggregates visible to the naked eye. For the case of MWCNT-PhOMe@PLLA films an almost linear trend in the optical absorption at 1000 nm (a wavelength where only CNSs absorb) can be observed for the first three wt% examined, as reported in Fig. 1b, while at higher wt% saturation of the signal was achieved, not allowing to extend the

extrapolation. For the other two functionalized-CNS@PLLA films only two points were measured due to saturated absorption at lower wt% as compared to MWCNT-PhOMe@PLLA films (see Fig. 1b). For the RGO-PhOMe@PLLA films the trend in absorbance was likely not linear, as inferred by guessing an absorbance of the 0.5 wt% film higher than four and therefore already out of a linear trend and a residual absorbance at 0 wt% CNS content (this last one resulting, at a lower extent, also for the other two types of functionalized-CNS@PLLA composites). Attempts to characterize the composites through FT-IR analysis failed due to the absence of any significant IR absorption feature in the functionalized-CNSs and to their low percentage in PLLA (only IR signals of the polymer were detected, with no shifts or intensity changes when going from the pure material to its composites).

The 5 wt% functionalized-CNS@PLLA composites were also produced in the form of nanofibers through the electrospinning technique (see the Experimental Section for details about the preparation), in order to investigate how such morphology would affect the electrical properties of our composite materials.

3.2 Thermal, mechanical and electrical characterization of the functionalized-CNS@PLLA composites

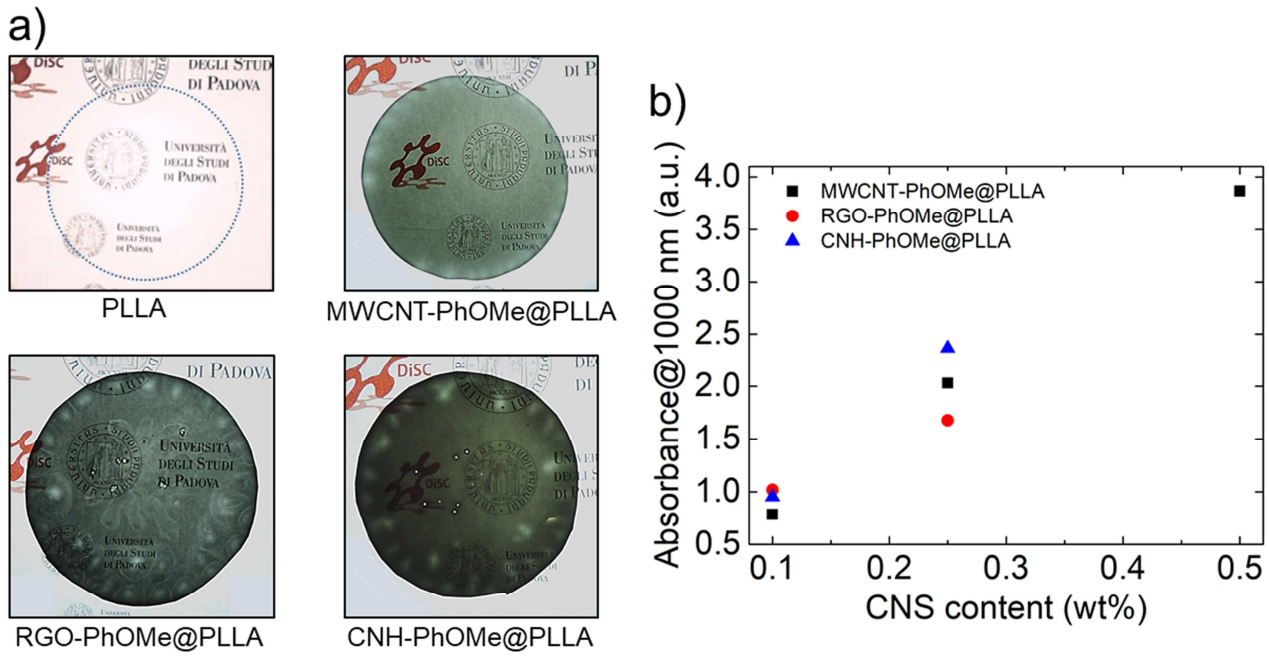

Fig. 1. a) Backlight photos of sample films (~6 cm diameter) of 0.1 wt% functionalized-CNS@PLLA films and of a pure PLLA (lighter color spots in the films are due to thinner areas and air bubbles which were discarded for all the following physical tests. They were present only in the 0.1 wt% samples, as shown by pictures of the other composites

reported in the S.I.). b) Absorbance at 1000 nm of nanocomposite films as a function of filler wt% (high filler concentrations giving signal saturation are omitted).

A further proof for the homogeneity of the dispersion of functionalized CNSs within the PLLA phase was obtained by considering the crystallization temperature (T_c) extrapolated from calorimetric data resulting after differential scanning calorimetry (DSC) analysis (see Fig.s S5, S6 and S7 for the DSC traces of the three types of functionalized-CNS@PLLA composites at all the studied concentrations, and Tables S2, S3 and S4 for a complete resume of calorimetric data).

Actually, T_c values are significantly influenced by the presence of well-dispersed nanofillers, which can act as nucleating agents, allowing crystallization to happen at lower temperatures (PLLA crystallizes on heating; cold crystallization) [14]. This was particularly evident in MWCNT-PhOMe@PLLA composites [59] for which an almost linear decrease of T_c was observed when increasing the quantity of nanofillers up to the 1 wt% limit (see Fig. 2b; Fig. 2a reports the detail of DSC traces in the region where polymer crystallization takes place).

A decrease in T_c was also recorded for the RGO-PhOMe@PLLA composites as a function of CNS concentration (Fig. S7), but it did not follow an almost linear regime as for MWCNTs. For CNH-PhOMe@PLLA composites an apparent opposite behavior was observed, since at lower CNH-PhOMe concentrations (up to 1 wt%) an increase in T_c was detected, followed by a decrease at the highest concentration examined (5 wt%, Fig. S6. For this sample, as well as for the 5 wt% MWCNT-PhOMe@PLLA sample, DSC were performed on more than one portion, to rule out inhomogeneity issues, but no differences among replicates were evidenced). The percent crystallinity of PLLA [60] decreases slightly after inclusion of all the types of nanofillers, but does not show a precise trend with increasing concentrations (see Table S2, S3 and S4). This might be somehow related to the analogous decrease in melting enthalpies in the composites compared to the pure polymer (see Table S2, S3 and S4). On the other hand, melting temperatures remain almost unvaried from case to case (see again Table S2, S3 and S4).

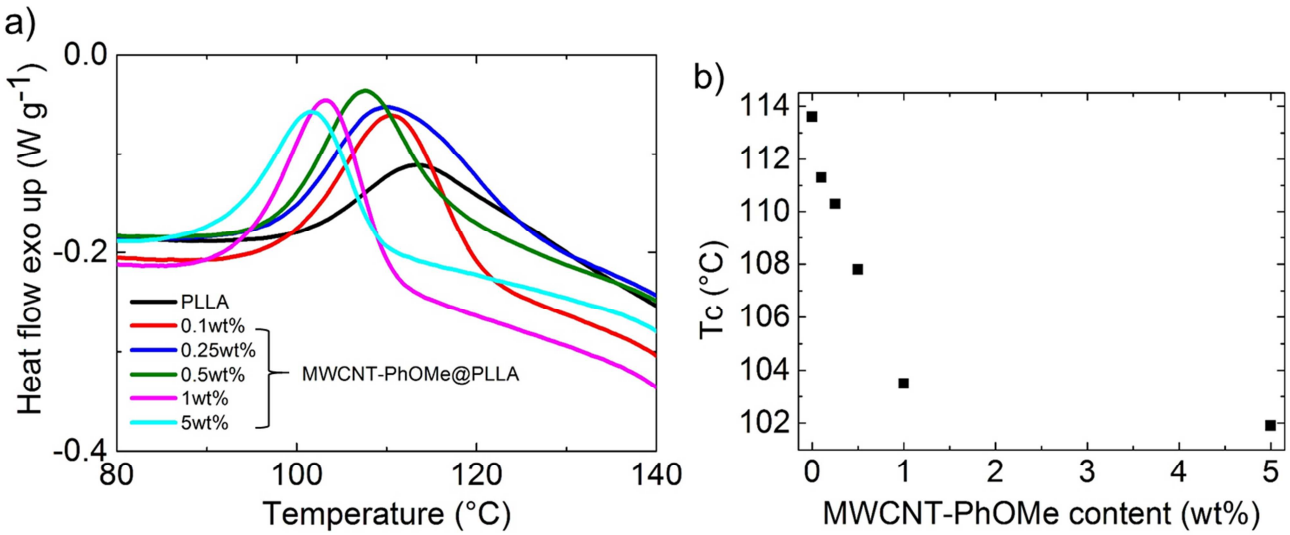

Fig. 2. a) Zoom of DSC traces (second heating scans after a previous heating-cooling cycle) of MWCNT-PhOMe@PLLA composites with five different filler concentrations and of pure PLLA in the zone where polymer crystallization takes place. b) Variation of T_c (taken at maximum of the curves in a) as a function of MWCNT-PhOMe in the composite.

The mechanical behavior of the functionalized-CNS@PLLA composites was investigated to determine the effect of the three nanofiller types at their different relative concentrations. The tensile strength was measured for all the examined materials on samples of the same size and thickness, except for the 5 wt% RGO-PhOMe@PLLA composite, which was too brittle to undergo mechanical testing (too brittle even for handling, as it can be somehow inferred from its picture in Fig. S4). Representative entire tensile stress-strain curves for each type of composite at the different filler content in PLLA are reported in the S.I. (Fig.s S8, S9 and S10); here we present the variation in Young's modulus (Fig. 3a) and the variation in the percentage of film deformation at the fracture point (Fig. 3b) as a function of the nanofiller concentration.

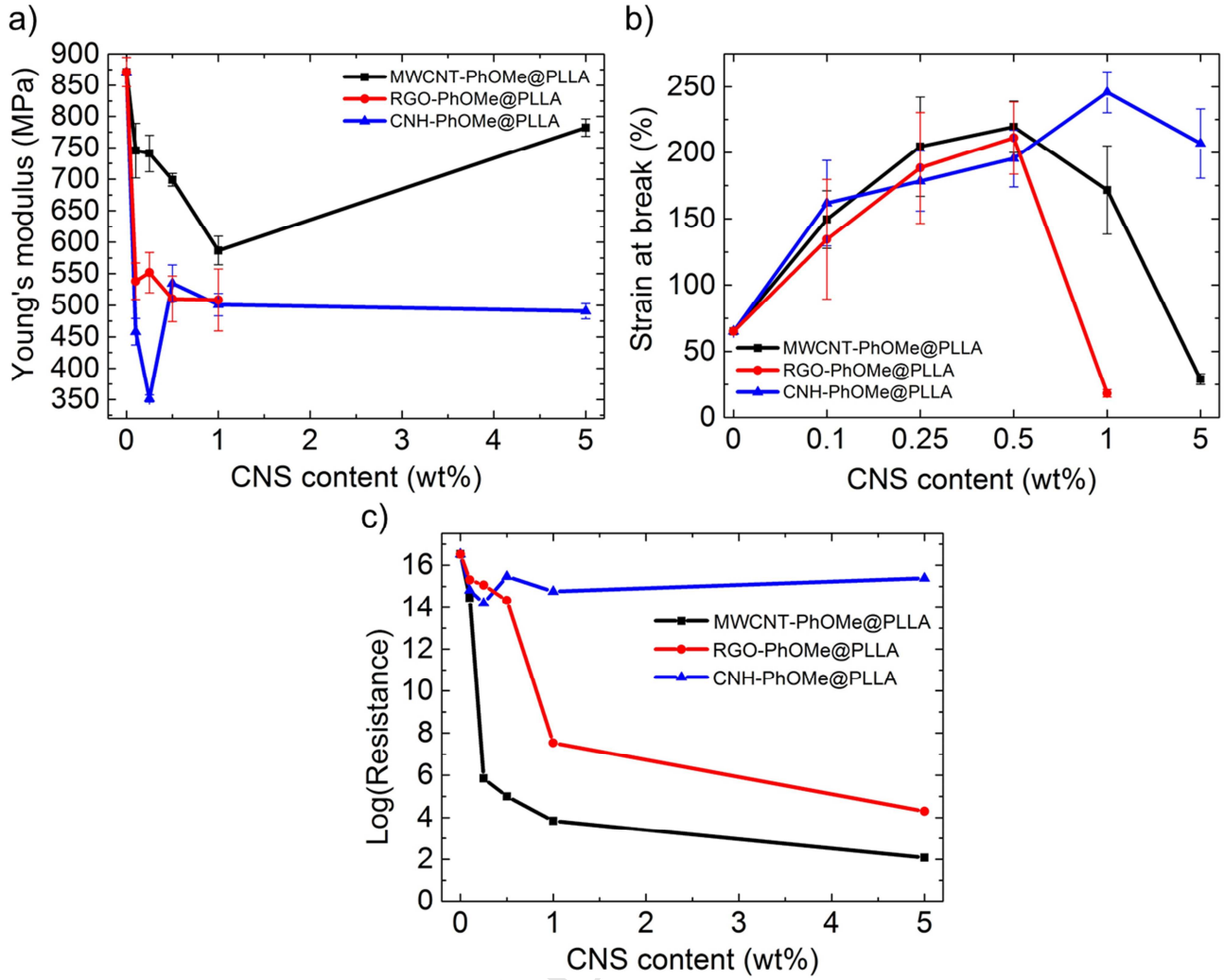

Fig. 3. a) Young's modulus, b) strain at break and c) electrical resistance in a logarithmic scale for functionalized-CNS@PLLA composites as a function of nanofiller concentration.

The elastic modulus changes significantly when functionalized-CNSs are dispersed in PLLA (Fig. 3a): the pure polymer has a modulus of 871 MPa, whereas the inclusion of small amounts of fillers (0.1 wt%) surprisingly drops it down to 745, 538 and 458 MPa for MWCNT-PhOMe, RGO-PhOMe and CNH-PhOMe, respectively. In general instead, loading polymers with stiffer fillers (normally in the pristine form and thus lacking functionalization) is expected to increase Young's modulus.[61] In the present case, functionalized-CNSs in PLLA behave more as plasticizers rather than as reinforcing agents. This has been observed before for poly(lactic-acid) phases plasticized with palm oil and filled with small amounts (up to 1wt%) of graphene nanoplatelets [62]. Since in our case no plasticizers have been added to PLLA, the effect must be likely driven by the presence of the *p*-methoxyphenyl substituents covalently bound to the CNSs, that allow their homogeneous dispersion within the polymeric phase. On the other hand, the formation of voids (defects) in the PLLA phase following nanofillers insertion, might be also the cause of lower stiffness in the composites compared to the pristine polymer. This aspect might be also connected with the

diminished crystallinity found in composites (see the previous discussion on DSC results). After the initial decrease at low CNS concentrations, Young's modulus undergoes a slight increase only at higher concentrations of the fillers for the case of MWCNT-PhOMe (at 5wt%) and CNH-PhOMe (at 0.5 wt%), but remains still lower than that of bare PLLA. However, the trend in elongations at the fracture point for the three types of composites (Fig. 3b) is noteworthy: the increase in ductility with increasing filler content, up to 0.5 wt% for both MWCNT-PhOMe and RGO-PhOMe, and up to 1 wt% for CNH-PhOMe, brings to final lengths at break which are 3-4 times longer than for PLLA. Unfortunately, in the RGO and MWCNT based composites, this effect drops down for higher concentrations, eventually leading to materials which are more fragile than bare PLLA at 1 wt% for RGO-PhOMe and 5 wt% for MWCNT-PhOMe. For the RGO-based composite at 5 wt% concentration it is not even possible to measure any tensile strength, because of the brittleness of the material, as already mentioned. Such a drop in ductility is instead not observed with CNH-PhOMe as a filler up to 5 wt%. While at lower concentrations CNS fillers are more homogeneously dispersed, it is reasonable to assume that at higher loadings they start to form larger aggregates, which affect the macroscopic ductility of the resulting composite. The overall mechanical response of the three types of composites must be significantly influenced by the type of contained nanofiller, as it was observed for the calorimetric behavior. Different behaviors among CNSs can be due, in particular, to their different size and shape, and can be driven by their different tendency to aggregate, though strongly mitigated by the covalent functionalization.

The bulk electrical properties of the functionalized-CNS@PLLA films were measured, showing again a behavior deeply influenced by the type of CNS used as nanofiller. In Fig. 3c the electrical resistance is shown as a function of the concentration of CNSs in PLLA. A percolation threshold at very low filler content is observed for the composites based on MWCNTs, with a significant change in resistance when moving from 0.1 to 0.25 wt%, corresponding to the formation of conductive networks. Indeed, it is known that CNTs are more effective than other standard fillers, such as carbon black, in conferring conductive properties to insulating polymers [63]. The fact that this happens at a low concentration of MWCNT-PhOMe deserves special attention [64], confirming that the CNS dispersion is optimized and the occurrence of aggregates is negligible, which is possible thanks to the organic functionalization that drives the homogeneous distribution of nanotubes among PLLA chains. The recorded conductivity also evidences that our functionalization approach avoided excessive modification of the CNT structure, which could result in the partial loss of the electronic properties of pristine nanotubes [65]. For the RGO-PhOMe@PLLA composites a percolation threshold was found between 0.5 and 1 wt% nanofiller concentration. These fillers appeared to be less effective in inducing electrical conductivity in PLLA, with electrical resistance

being 2 order of magnitudes higher than that reached with CNTs at the maximum concentration (5 wt%). On the other hand, with the CNH-PhOMe fillers no percolation threshold was observed at the considered CNS concentrations, demonstrating again that the differences in nanomorphology among the components largely determine the macroscopic behavior. Indeed CNH species, existing in their aggregated "dahlia-like" globular shape [47], have sizes of 100 nm (see TEM images of fibers containing them in Fig. S11b in the S.I.) and are therefore not likely to form conductive pathways within the polymer phase at such low concentrations.

3.3 Atomic force microscopy characterization of the functionalized-CNS@PLLA composites

In order to electrically characterize the composites at the single filler size resolution, the materials were also investigated by means of AFM techniques. Only composites with the highest filler concentration (5 wt%) were considered.

The conductance was addressed by means of conductive AFM (CAFM) measurements. The film of bare PLLA did not show any measurable current, as expected, and the same occurred also for the CNH-PhOMe@PLLA composite film, even when probed at several different positions on its surface and with different contact forces (see details in the S.I.). This confirmed the data obtained through the macroscopic electrical characterization. The samples of MWCNT-PhOMe@PLLA and RGO-PhOMe@PLLA exhibited instead measurable currents. Representative current images for the MWCNT-PhOMe@PLLA and for the RGO-PhOMe@PLLA samples are presented in Fig. 4b and 4d, respectively (Fig. 4a and 4c report the corresponding topography).

When considering for example the MWCNT-PhOMe@PLLA composite film (Fig. 4b), one can see that the current image is partly correlated with the surface topography, as few high regions show no current (see filled arrows). However, these are real effects associated with the feature contents and not topographical artifacts. The different compositional contents in the aforementioned tall features is also apparent in other surrounding regions with similar low current level (black areas) yet without outstanding heights (see void arrows). Obviously, independently on their height, areas of the films exist which are locally devoid of the CNS fillers imparting conductance to the composite. Conversely, the conducting regions emerging in Fig. 4b show a finer structure (down to the single pixel size i.e. ~40 nm) than in Fig. 4d. Indeed, in the former case they are likely associated with smaller sizes of the carbon-based fillers (single MWCNTs or bundles of few of them), whereas in Fig. 4d the bright regions include several adjacent pixels up to ~2 μm linear size (see the arrowed zone) which are likely associated with sparse RGO flakes.

Fig. 4 further shows that, under the same conditions of vertical force (~18 nN) and bias (+1 V), the current levels observed on the MWCNT-PhOMe@PLLA film surface are higher than those for the

RGO-PhOMe@PLLA one (see the vertical scale bar of the color palettes). Additionally, the total conductive area is higher for the MWCNT-PhOMe@PLLA composite, (17±5 % versus 7±4 % of the RGO containing composite film). When considering the means of the current levels on the different images of the samples, and averaging them, from the applied sample voltage (+1 V) resistance values of 2.6 ± 1.2 MΩ and 530 ± 230 MΩ are obtained for the MWCNT-PhOMe@PLLA and the RGO-PhOMe@PLLA sample, respectively, which can be considered representative of the whole films. These values are in a similar ratio (about 200×) to that of film resistances measured macroscopically (see Fig. 3c), yet are both shifted to approximately 4 orders of magnitude higher values. This likely depends on the very small contact area of the AFM tip, for the considered technique, at the limited vertical force used (see details in the S.I.). The agreement between electrical measurements made at the macro and nanoscale is a proof of the good homogeneity achieved in dispersing the functionalized-CNS within the polymer matrix.

In Fig. 4e also single I-V curves typical of points in which conduction occurred (i.e. within bright regions in Fig.s 4a and b) have been plotted. One can see that the composite film with CNT fillers exhibit an almost 'metallic' behavior (straight Ohmic I-V profile), while the RGO film shows a passive region close to zero bias (sigmoidal profile), more similar to a semiconductor. An analogous difference in current values (about two orders of magnitude) between the two different samples is observed as described above, in favor of the MWCNT-PhOMe@PLLA film. When only the same range of the I-V curves as used in the current images (±1 V) is considered, the following values of resistance are obtained, from a linear fit: 0.48 MΩ for the MWCNT-PhOMe@PLLA sample and 26.7 MΩ for the RGO-PhOMe@PLLA sample. These values are higher than the means on the image areas (affected by the 'dark' regions of no current, so weighted with the coverage coefficients), yet are roughly in the same ratio of approximately 200× in favor of the CNT containing composite.

Finally, we investigated with CAFM the conductive properties of the functionalized-CNS@PLLA composites in the form of nanofibers, obtained with the electrospinning technique, as reported[14] (for transmission electron microscopy images of the fibers see Fig. S11 in the S.I.). This morphology was selected in order to study the electrical properties of the composites in nanoscale-confined model systems, along a single direction. It is worthy to mention that the electrical conductivity measurements carried out on films (see previous section) would hardly apply to fibrous phases, because of the very low density of the material preventing a proper contact with the electrodes. In Fig. 4f a CAFM image of a single MWCNT-PhOMe@PLLA nanofiber is shown. The current level has been rendered as the color, overlaid on the 3D profile of the height. For composite nanofibers, the CNT based sample was the only one which allowed current imaging, while in this

form also the RGO-based composite did not show any conductivity. This can be justified by considering that, for the same filler concentration, percolation along a narrow

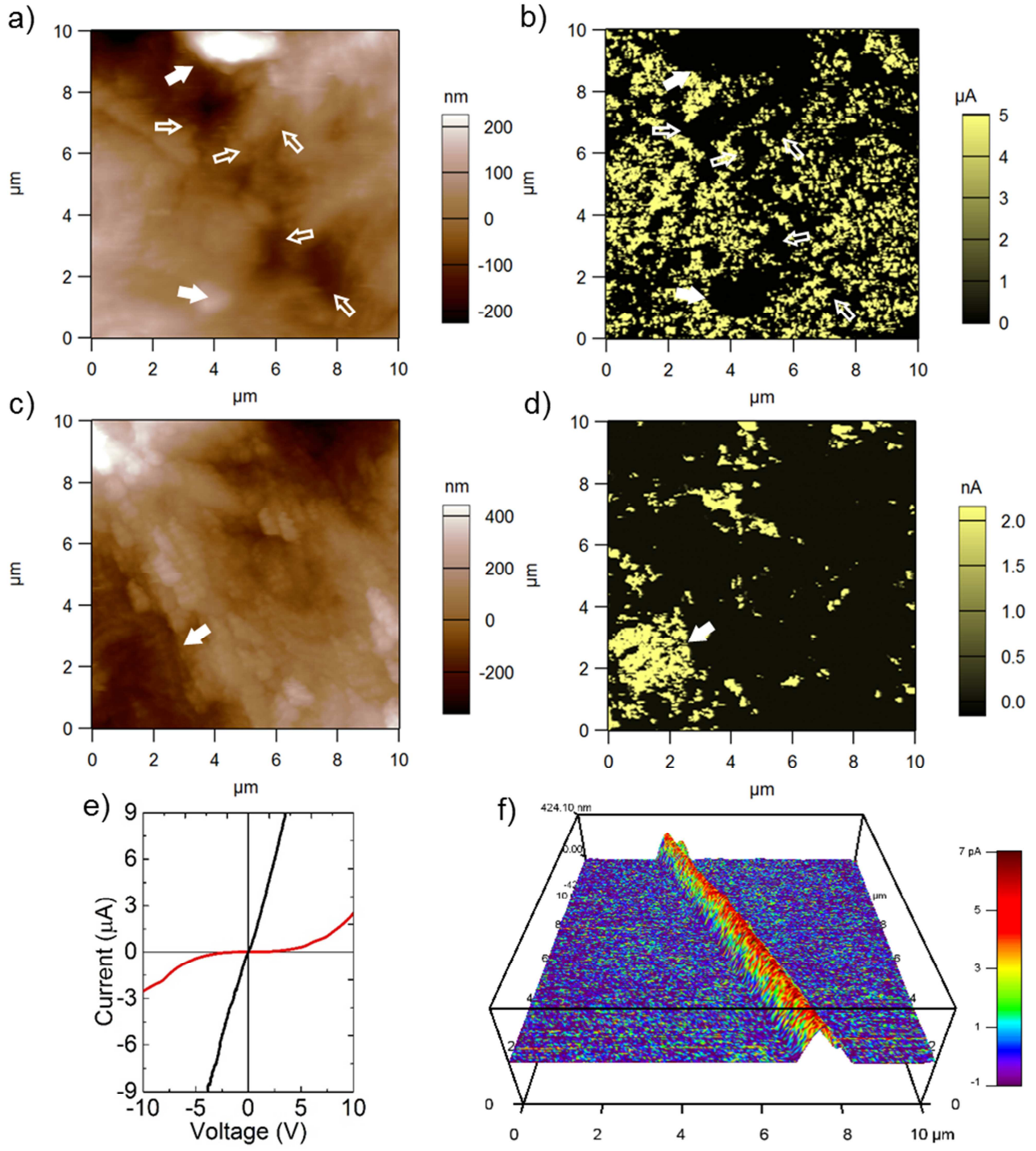

Fig. 4. a-d) Representative CAFM images of films of a,b) MWCNT-PhOMe@PLLA and c,d) RGO-PhOMe@PLLA; a,c) topography, b,d) current images (at +1 V). d) I-V characteristic curves obtained at conductive points on the two samples of composite films. Black curve: MWCNT-PhOMe@PLLA film; red curve: RGO-PhOMe@PLLA film. f) 3D rendering of a current image taken on a MWCNT-PhOMe@PLLA electrospun nanofiber, with the current overlaid as a color onto the topographic 3D profile.

conductor such as a nanofiber (200-600 nm diameter) is more difficult and is detected in the present case only for monodimensional conductive fillers as CNTs. Also the geometry of the CAFM contact was significantly different in this case, in-plane along the fiber axis and not through the fiber towards the substrate. Actually, in the case of fibers, the substrate used was insulating, which allows to obtain a typical value of fiber conductance. When the resistance is calculated, a value of ~7.1 GΩ is obtained, another factor 300× higher than what measured for the film of the same composite, and close to the lower detection limit level of the setup (mean current along fiber axis in Fig. 4f is 4.8 pA). In order to support the electrical characterization of the different composites, we carried out AFM electrostatic measurements (scanning Kelvin probe microscopy –SKPM- and/or electrostatic force microscopy –EFM-) on the functionalized-CNS@PLLA composite nano-confined systems with fibrous morphology. These AFM techniques are based on potential contrast due to accumulation of electrical charges, instead of their flow within a current, as for CAFM. Therefore, insulating fiber portions, not allowing the charge to be drained away, are expected to exhibit stronger contrast. This was actually observed with fibers of bare PLLA (see Fig. S12a and b). The typical nature of the electrostatic contrast is apparent when noticing that the bright regions spread around the physical lateral extension of the fibers, which was not the case for the current in Fig. 4f. Similar results have been obtained also for the other samples of insulating (i.e. non-conductive) fibers (namely those containing RGO and CNH fillers). For the fibrous sample containing MWCNTs instead, in few cases, we observed fibers that looked from less bright (i.e. with only some degree of conduction, Fig. S12c and d) on to completely dark (i.e. completely conductive, Fig. S12e and f). Unfortunately, it was not possible to acquire CAFM and SKPM/EFM images simultaneously on the same fiber portion, because the two classes of techniques require different probe-holders. An interesting representative SKPM image of the MWCNT-PhOMe@PLLA fibers is shown in Fig. 5. In Fig. 5a a region is evident where several fibers cross each other. In the corresponding surface potential (SKPM) image of Fig. 5b three different levels appear, namely an intermediate level background (associated with the substrate); a higher level (bright regions) spreading around the fibers (the typical bleeding effect of electrostatic charging); and a negative contrast (black) region localized only on some positions along the fibers, which can be associated with the functionalized MWCNT fillers (see TEM images in Fig. S11a for comparison). Such three regions are more clearly represented in Fig. 5c, where the same maps of topography (height) and surface potential and as in a) and b) have been rendered again in 3D fashion, using a multicolor palette to segment the above-mentioned regions in different levels associated with red, green and blue colors, respectively.

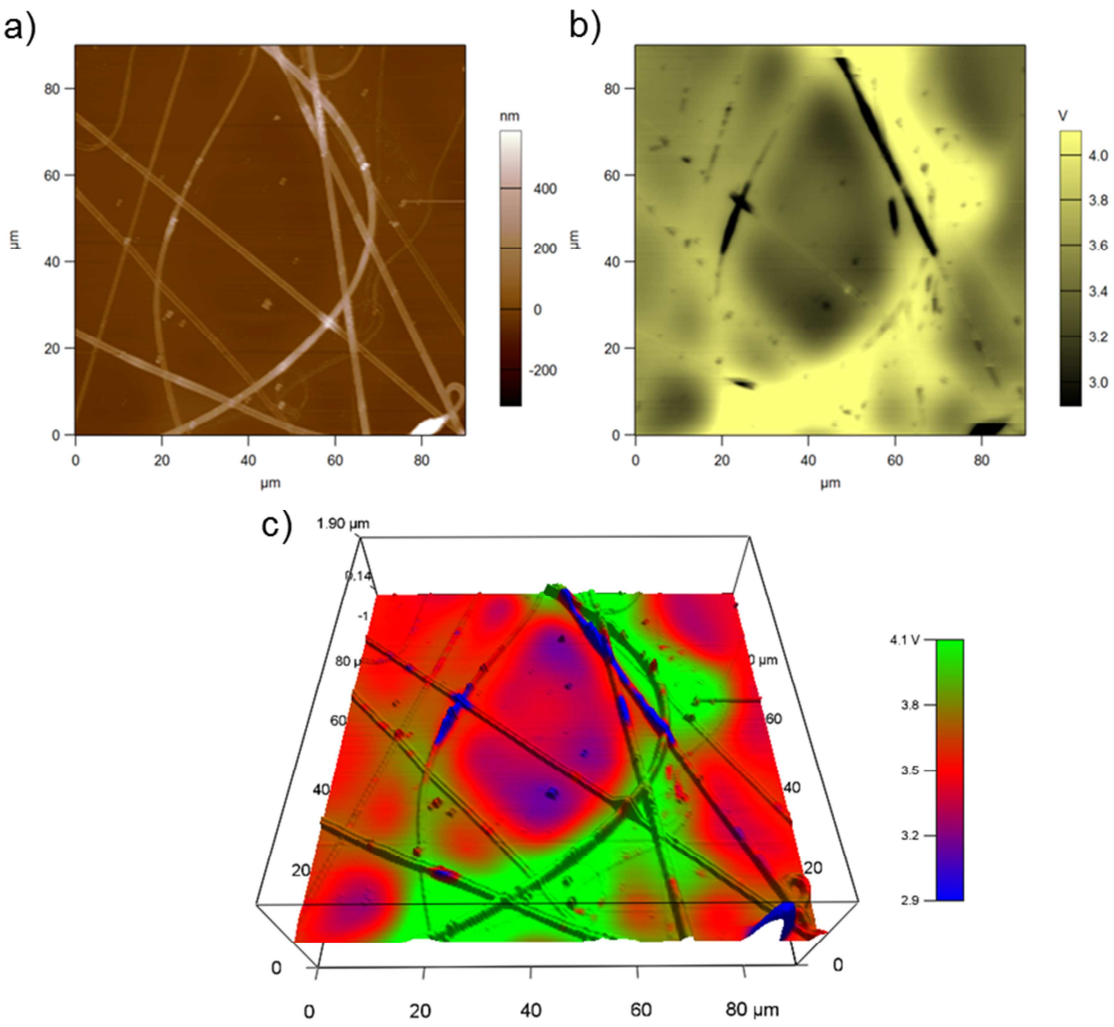

Fig. 5. Large-area SKPM images of a sample of MWCNT-PhOMe@PLLA composite fibers, a) topography; b) surface potential; c) 3D topography of a) 'colored' with the surface potential in b).

As a final step of surface characterization of the functionalized-CNS@PLLA composites, the roughness of the film samples has been assessed by standard AFM (in non-contact mode). In Fig. S14 in the S.I. the 2D roughness amplitude parameter S_q, is presented. The two composite materials based on CNH and RGO fillers result in films with higher surface roughness (S_q~155 nm), whereas the composite based on MWCNTs is smoother, on the same level as the film of bare PLLA (S_q~70 nm). The differences between the two groups are statistically significant ($p<0.05$). Therefore, the well-dispersed MWCNT-PhOMe fillers provide a good uniformity in the overall electrical properties, resulting in a percolation network that endows the films with a good electrical conductivity and, in addition, turns out to determine the least amount of surface roughening, as compared to the bare polymer film.

3.4 Biocompatibility of the functionalized-CNS@PLLA composites

The functionalized-CNS@PLLA films were tested for biocompatibility by employing them as scaffolds for the growth of SH-SY5Y cells. For both cell death and cell proliferation assays, only two percentages per each type of CNS filler were selected, namely a lower one (0.25 wt%) and a higher one (5 wt%). Together with control cells grown onto poly-L-lysine or onto FDA-certified PLLA polymer, which has an already established usage in regenerative medicine, CNTs at 0.25 wt% also represent a 'positive control' for biocompatibility, as this concentration was well characterized and proved fully biocompatible (when dispersed in either PLLA films of electrospun PLLA) [13-15]. In this work, CNTs concentrations up to 5% and novel nanocomposites including RGO or CNHs are tested for the first time with SH-SY5Y cells, to check whether viability values are kept. According to previous studies, cell viability was evaluated at 24 and 72 hours combining evaluation of cell death to proliferation data, in order to properly consider factors underlying cell viability. Cells grown onto 0.25 or 5% functionalized-CNS@PLLA films showed viability values in the same range as control and PLLA samples (Fig. 6a) and no meaningful effect on cell proliferation (Fig. 6b), thus demonstrating biocompatibility is kept and the potential cytotoxicity of the three types of CNSs is prevented when employing them well functionalized and dispersed within a biocompatible polymer matrix.

3.5 Discussion

The functionalized-CNS@PLLA composites were thoroughly characterized in their thin film forms by assessing the variation in thermal, mechanical and electrical properties as a function of CNS loading over a range between 0.1 wt% and 5 wt%. The homogeneity of the CNS nanofillers dispersion within the polymer phase was stated, particularly for the MWCNT-based samples for which an almost linear trend was found in the decrease of the crystallization temperature of the polymer as a function of the increased filler concentration.

The mechanical properties were found to be highly influenced by the presence of the *p*-methoxyphenyl functional groups covalently bound to the CNS surfaces, which confer to the fillers an unusual character of plasticizing agents rather than of reinforcing ones. The ductility of the composites is extremely improved with respect to bare PLLA for concentrations of CNSs around 0.5-1 wt%, even though for RGO-based samples the limits to obtain an improved plasticity are lower than for MWCNT and CNH-based samples, with the 5 wt% concentration already too high to furnish a durable material.

Electrical percolation in the composites was found to take place only with MWCNT and RGO fillers, within the range of concentrations considered. Thresholds were differently located for the two cases, with the MWCNT-PhOMe@PLLA composites showing a sharp increase in conductivity

at a lower CNS concentration with respect to RGO-PhOMe@PLLA. The extent of conductivity after the

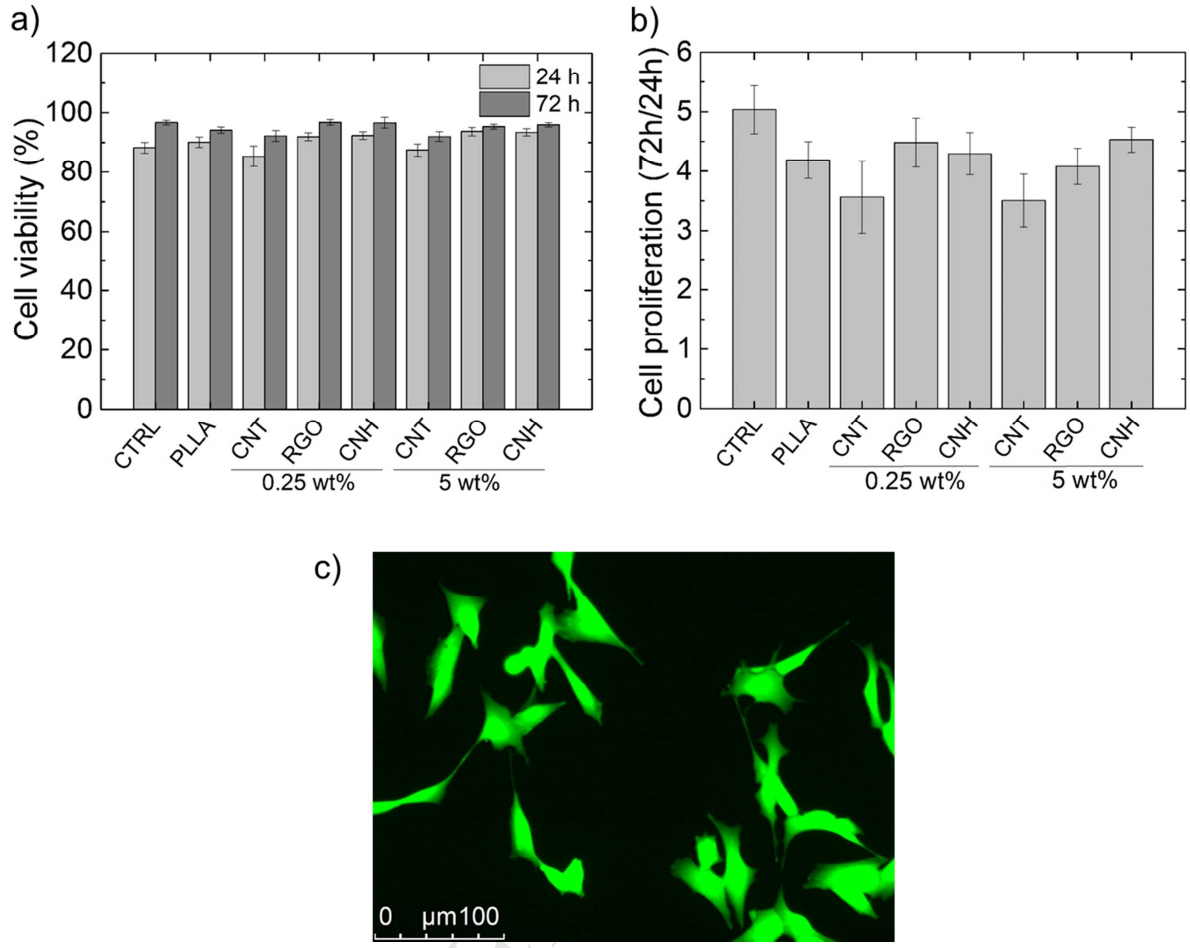

Fig. 6. Percentage of viability a) or proliferation b) for SH-SY5Y cells grown onto control (poly-L-lysine coated) wells, pure PLLA film or functionalized-CNS@PLLA films. Data represents the mean ± SEM of four independent experiments performed in duplicate. An example c) of SH-SY5Y cells grown on MWCNT-PhOMe@PLLA film at 72 hour. Cells are stained with Calcein-AM. Image magnification is 20X. No meaningful difference is observed in images with RGO-PhOMe@PLLA and CNH-PhOMe@PLLA.

percolation threshold was also significantly higher for the former as compared to the latter. A strong influence of the filler dimensionality on the electrical behavior of the composite is evident: monodimensional CNSs like MWCNTs are able to arrange in conductive domains within polymer chains much more effectively than bidimensional CNSs like RGO. Finally, zero-dimensional species such as CNHs likely require high concentrations to give rise to conductive pathways within an insulating matrix. The superior ability of CNTs to form conductive networks over a long distance is further confirmed by the CAFM data obtained on both film surfaces and along single nanofibers. Particularly for these last ones, a measurable current could be detected only for CNT-based samples. Also considering the increasing interest on nanofibrous biomedical materials [66, 67], the

ability to originate long range and directional percolation pathways might be promising to provide next scaffold design with a selective guidance to neurites elongation.

4. Conclusions

In this work a thorough assessment of the physical properties of functionalized-CNS@PLLA composites is essayed, both at the macroscopic level and at the nanoscale, directly on surfaces, which are the part of the samples directly responsible for the interaction with living cells. The analysis is carried out with the awareness that a combination of stimuli coming from the substrate is responsible for the growth and differentiation of cells, including electrical, mechanical and topographic cues and thus will act as a guidance for future studies of neuritogenesis. These characterization efforts are addressed at increasing the understanding about physical properties driving cellular processes *in vitro* at first instance. These results also provide a basic set of information for the design and selection of optimized scaffolds to be tested *in vivo*, aiming at the future development of biomedical devices and implants for tissue engineering applications.

Acknowledgements

The authors acknowledge the financial support from University of Padova (Project PRAT2015 CPDA151948 to FF and contract P-DiSC #05BIRD2016-UNIPD to EM). They also thank Dr. Giorgia Scapin for helpful information and suggestions.

References

[1] S. Bhattacharya, S.K. Samanta, Soft-Nanocomposites of Nanoparticles and Nanocarbons with Supramolecular and Polymer Gels and Their Applications, Chem. Rev. 116(19) (2016) 11967-12028.
[2] Z. Spitalsky, D. Tasis, K. Papagelis, C. Galiotis, Carbon nanotube–polymer composites: Chemistry, processing, mechanical and electrical properties, Progr. Polym. Sci. 35(3) (2010) 357-401.
[3] A. Sherif, M. Qingshi, Z. Liqun, Z. Izzuddin, M. Peter, M. Jun, Elastomeric composites based on carbon nanomaterials, Nanotechnology 26(11) (2015) 112001.
[4] M. Wang, X. Duan, Y. Xu, X. Duan, Functional Three-Dimensional Graphene/Polymer Composites, ACS Nano 10(8) (2016) 7231-7247.
[5] J. Du, H.-M. Cheng, The Fabrication, Properties, and Uses of Graphene/Polymer Composites, Macromol. Chem. Phys. 213(10-11) (2012) 1060-1077.
[6] Y. Zhu, C. Romain, C.K. Williams, Sustainable polymers from renewable resources, Nature 540(7633) (2016) 354-362.
[7] C. Goncalves, I.C. Goncalves, F.D. Magalhaes, A.M. Pinto, Poly(lactic acid) Composites Containing Carbon-Based Nanomaterials: A Review, Polymers 9(7) (2017).
[8] T. Gatti, N. Vicentini, M. Mba, E. Menna, Organic Functionalized Carbon Nanostructures for Functional Polymer-Based Nanocomposites, Eur. J. Org. Chem. 2016(6) (2016) 1071-1090.
[9] F.M. Michael, M. Khalid, R. Walvekar, C.T. Ratnam, S. Ramarad, H. Siddiqui, M.E. Hoque, Effect of nanofillers on the physico-mechanical properties of load bearing bone implants, Mater. Sci. Eng. C-Mater. Biol. Appl. 67 (2016) 792-806.
[10] M.S. Mozumder, A. Mairpady, A.H.I. Mourad, Polymeric nanobiocomposites for biomedical applications, J. Biomed. Mater. Res. Part B 105(5) (2017) 1241-1259.

[11] A.J.T. Teo, A. Mishra, I. Park, Y.-J. Kim, W.-T. Park, Y.-J. Yoon, Polymeric Biomaterials for Medical Implants and Devices, ACS Biomater. Sci. Eng. 2(4) (2016) 454-472.
[12] B.Q.Y. Chan, Z.W.K. Low, S.J.W. Heng, S.Y. Chan, C. Owh, X.J. Loh, Recent Advances in Shape Memory Soft Materials for Biomedical Applications, ACS Appl. Mater. Interfaces 8(16) (2016) 10070-10087.
[13] G. Scapin, P. Salice, S. Tescari, E. Menna, V. De Filippis, F. Filippini, Enhanced neuronal cell differentiation combining biomimetic peptides and a carbon nanotube-polymer scaffold, Nanomed.-Nanotechnol. Biol. Med. 11(3) (2015) 621-632.
[14] N. Vicentini, T. Gatti, P. Salice, G. Scapin, C. Marega, F. Filippini, E. Menna, Covalent functionalization enables good dispersion and anisotropic orientation of multi-walled carbon nanotubes in a poly(l-lactic acid) electrospun nanofibrous matrix boosting neuronal differentiation, Carbon 95 (2015) 725-730.
[15] G. Scapin, T. Bertalot, N. Vicentini, T. Gatti, S. Tescari, V. De Filippis, C. Marega, E. Menna, M. Gasparella, P.P. Parnigotto, R. Di Liddo, F. Filippini, Neuronal commitment of human circulating multipotent cells by carbon nanotube-polymer scaffolds and biomimetic peptides, Nanomedicine 11(15) (2016) 1929-1946.
[16] M. Kharaziha, S.R. Shin, M. Nikkhah, Tough and flexible CNT-polymeric hybrid scaffolds for engineering cardiac constructs, Biomaterials 35 (2014).
[17] S. Soltani, M. Ebrahimian-Hosseinabadi, A. Zargar Kharazi, Chitosan/graphene and poly(D, L-lactic-co-glycolic acid)/graphene nano-composites for nerve tissue engineering, Tissue Eng. Regen. Med. 13(6) (2016) 684-690.
[18] A. Gupta, T.A. Liberati, S.J. Verhulst, B.J. Main, M.H. Roberts, A.G.R. Potty, T.K. Pylawka, S.F. El-Amin III, Biocompatibility of single-walled carbon nanotube composites for bone regeneration, Bone and Joint Res. 4(5) (2015) 70-77.
[19] E. Murray, S. Sayyar, B.C. Thompson, R. Gorkin Iii, D.L. Officer, G.G. Wallace, A bio-friendly, green route to processable, biocompatible graphene/polymer composites, RSC Adv. 5(56) (2015) 45284-45290.
[20] S. Sayyar, E. Murray, B.C. Thompson, J. Chung, D.L. Officer, S. Gambhir, G.M. Spinks, G.G. Wallace, Processable conducting graphene/chitosan hydrogels for tissue engineering, J. Mater. Chem. B 3(3) (2015) 481-490.
[21] M. Silva, S.G. Caridade, A.C. Vale, E. Cunha, M.P. Sousa, J.F. Mano, M.C. Paiva, N.M. Alves, Biomedical films of graphene nanoribbons and nanoflakes with natural polymers, RSC Adv. 7(44) (2017) 27578-27594.
[22] A. Motealleh, N.S. Kehr, Nanocomposite Hydrogels and Their Applications in Tissue Engineering, Adv. Healthc. Mater. 6(1) (2017).
[23] D.P. Li, T.J. Liu, X.Q. Yu, D. Wu, Z.Q. Su, Fabrication of graphene-biomacromolecule hybrid materials for tissue engineering application, Polym. Chem. 8(30) (2017) 4309-4321.
[24] T.H. Kim, T. Lee, W.A. El-Said, J.W. Choi, Graphene-Based Materials for Stem Cell Applications, Materials 8(12) (2015) 8674-8690.
[25] K.Y. Yasoda, K.N. Bobba, D. Nedungadi, D. Dutta, M.S. Kumar, N. Kothurkar, N. Mishra, S. Bhuniya, GSH-responsive biotinylated poly(vinyl alcohol)-grafted GO as a nanocarrier for targeted delivery of camptothecin, RSC Adv. 6(67) (2016) 62385-62389.
[26] A. Antonucci, J. Kupis-Rozmyslowicz, A.A. Boghossian, Noncovalent Protein and Peptide Functionalization of Single-Walled Carbon Nanotubes for Biodelivery and Optical Sensing Applications, ACS Appl. Mater. Interfaces 9(13) (2017) 11321-11331.
[27] M. Irimia-Vladu, E.D. Głowacki, G. Voss, S. Bauer, N.S. Sariciftci, Green and biodegradable electronics, Mater. Today 15(7–8) (2012) 340-346.
[28] Q. Zhang, W. Wei, J. Li, J. Wei, J. Guo, Insertion of a biocompatible polymer bewteen graphene and silver nanowires for novel flexible transparent electrode, Synth. Met. 221 (2016) 192-200.
[29] T. Zhang, J. Liu, C. Wang, X. Leng, Y. Xiao, L. Fu, Synthesis of graphene and related two-dimensional materials for bioelectronics devices, Biosens. Bioelectron. 89, Part 1 (2017) 28-42.
[30] M. Hasanzadeh, F. Mokhtari, N. Shadjou, A. Eftekhari, A. Mokhtarzadeh, V. Jouyban-Gharamaleki, S. Mahboob, Poly arginine-graphene quantum dots as a biocompatible and non-toxic nanocomposite: Layer-by-layer electrochemical preparation, characterization and non-invasive malondialdehyde sensory application in exhaled breath condensate, Mat. Sci. Eng. C 75 (2017) 247-258.
[31] F. Lamberti, S. Giulitti, M. Giomo, N. Elvassore, Biosensing with electroconductive biomimetic soft materials, J. Mater. Chem. B 1(38) (2013) 5083-5091.

[32] Y. Zhou, X.X. Jing, Y. Chen, Material chemistry of graphene oxide-based nanocomposites for theranostic nanomedicine, J. Mater. Chem. B 5(32) (2017) 6451-6470.
[33] J. Pan, F.R. Li, J.H. Choi, Single-walled carbon nanotubes as optical probes for bio-sensing and imaging, J. Mater. Chem. B 5(32) (2017) 6511-6522.
[34] J. Bartelmess, S.J. Quinn, S. Giordani, Carbon nanomaterials: multi-functional agents for biomedical fluorescence and Raman imaging, Chem. Soc. Rev. 44(14) (2015) 4672-4698.
[35] C. Hu, Z. Li, Y. Wang, J. Gao, K. Dai, G. Zheng, C. Liu, C. Shen, H. Song, Z. Guo, Comparative assessment of the strain-sensing behaviors of polylactic acid nanocomposites: reduced graphene oxide or carbon nanotubes, J. Mater. Chem. C 5(9) (2017) 2318-2328.
[36] L. Hines, K. Petersen, G.Z. Lum, M. Sitti, Soft Actuators for Small-Scale Robotics, Adv. Mater. 29(13) (2017) 1603483-n/a.
[37] J. Ahmed, M. Mulla, Y.A. Arfat, L.A. Thai T, Mechanical, thermal, structural and barrier properties of crab shell chitosan/graphene oxide composite films, Food Hydrocoll. 71 (2017) 141-148.
[38] N. Pal, P. Dubey, P. Gopinath, K. Pal, Combined effect of cellulose nanocrystal and reduced graphene oxide into poly-lactic acid matrix nanocomposite as a scaffold and its anti-bacterial activity, Int. J. Biol. Macromol. 95 (2017) 94-105.
[39] N. Yan, F. Capezzuto, M. Lavorgna, G.G. Buonocore, F. Tescione, H. Xia, L. Ambrosio, Borate cross-linked graphene oxide-chitosan as robust and high gas barrier films, Nanoscale 8(20) (2016) 10783-10791.
[40] K. Zhang, J.Y. Lim, H.J. Choi, J.H. Lee, W.J. Choi, Ultrasonically prepared polystyrene/multi-walled carbon nanotube nanocomposites, J. Mater. Sci. 48(8) (2013) 3088-3096.
[41] G. Pagani, M.J. Green, P. Poulin, M. Pasquali, Competing mechanisms and scaling laws for carbon nanotube scission by ultrasonication, Proc. Natl. Acad. Sci. U. S. A. 109(29) (2012) 11599-11604.
[42] M.D. Rossell, C. Kuebel, G. Ilari, F. Rechberger, F.J. Heiligtag, M. Niederberger, D. Koziej, R. Erni, Impact of sonication pretreatment on carbon nanotubes: A transmission electron microscopy study, Carbon 61 (2013) 404-411.
[43] J. Stegen, Mechanics of carbon nanotube scission under sonication, J. Chem. Phys. 140(24) (2014).
[44] S. Barrau, P. Demont, E. Perez, A. Peigney, C. Laurent, C. Lacabanne, Effect of Palmitic Acid on the Electrical Conductivity of Carbon Nanotubes−Epoxy Resin Composites, Macromolecules 36(26) (2003) 9678-9680.
[45] D. Tasis, N. Tagmatarchis, A. Bianco, M. Prato, Chemistry of Carbon Nanotubes, Chem. Rev. 106(3) (2006) 1105-1136.
[46] V. Georgakilas, M. Otyepka, A.B. Bourlinos, V. Chandra, N. Kim, K.C. Kemp, P. Hobza, R. Zboril, K.S. Kim, Functionalization of Graphene: Covalent and Non-Covalent Approaches, Derivatives and Applications, Chem. Rev. 112(11) (2012) 6156-6214.
[47] N. Karousis, I. Suarez-Martinez, C.P. Ewels, N. Tagmatarchis, Structure, Properties, Functionalization, and Applications of Carbon Nanohorns, Chem. Rev. 116(8) (2016) 4850-4883.
[48] T. Gatti, G. Girardi, N. Vicentini, R. Brandiele, M. Wirix, C. Durante, E. Menna, Physico-Chemical, Electrochemical and Structural Insights Into Poly(3,4-ethylenedioxythiophene) Grafted from Molecularly Engineered Multi-Walled Carbon Nanotube Surfaces, J. Nanosci. Nanotechnol. 18(2) (2018) 1006-1018.
[49] P. Salice, E. Fabris, C. Sartorio, D. Fenaroli, V. Figà, M.P. Casaletto, S. Cataldo, B. Pignataro, E. Menna, An insight into the functionalisation of carbon nanotubes by diazonium chemistry: Towards a controlled decoration, Carbon 74(0) (2014) 73-82.
[50] B. Debalina, N. Vaishakh, M. Jagannatham, K. Vasanthakumar, N.S. Karthiselva, R. Vinu, P. Haridoss, S.R. Bakshi, Effect of different nano-carbon reinforcements on microstructure and properties of TiO2 composites prepared by spark plasma sintering, Ceram. Int. 42(12) (2016) 14266-14277.
[51] D. Iglesias, S. Bosi, M. Melchionna, T. Da Ros, S. Marchesan, The Glitter of Carbon Nanostructures in Hybrid/Composite Hydrogels for Medicinal Use, Curr. Top. Med. Chem. 16(18) (2016) 1976-1989.
[52] M. Radtke, A. Ignaszak, Grafting of the carbon allotropes and polypyrrole via a Kevlar-type organic linker: the correlation of carbon structure/morphology with electrochemistry of the composite electrode, Mater. Renew. Sustain. Energy 6(1) (2017).
[53] T. Gatti, S. Casaluci, M. Prato, M. Salerno, F. Di Stasio, A. Ansaldo, E. Menna, A. Di Carlo, F. Bonaccorso, Boosting Perovskite Solar Cells Performance and Stability through Doping a Poly-3(hexylthiophene) Hole

Transporting Material with Organic Functionalized Carbon Nanostructures, Adv. Funct. Mater. 26(41) (2016) 7443-7453.
[54] T. Gatti, N. Manfredi, C. Boldrini, F. Lamberti, A. Abbotto, E. Menna, A D-π-A organic dye – Reduced graphene oxide covalent dyad as a new concept photosensitizer for light harvesting applications, Carbon 115 (2017) 746-753.
[55] P. Guarracino, T. Gatti, N. Canever, M. Abdu-Aguye, M.A. Loi, E. Menna, L. Franco, Probing photoinduced electron-transfer in graphene-dye hybrid materials for DSSC, Phys. Chem. Chem. Phys. 19(40) (2017) 27716-27724.
[56] L. Gabrielli, G. Altoè, M. Glaeske, S. Juergensen, S. Reich, A. Setaro, E. Menna, F. Mancin, T. Gatti, Controlling the Decoration of the Reduced Graphene Oxide Surface with Pyrene-Functionalized Gold Nanoparticles, physica status solidi (b) 254(11) (2017) 1700281.
[57] R.A. Ross, B.A. Spengler, J.L. Biedler, Coordinate Morphological and Biochemical Interconversion of Human Neuroblastoma Cells2, JNCI-J Natl. Cancer I. 71(4) (1983) 741-747.
[58] J.L. Bahr, J.M. Tour, Covalent chemistry of single-wall carbon nanotubes, J. Mater. Chem. 12(7) (2002) 1952-1958.
[59] Z.-J. Zhang, W. Cui, H. Xu, L. Xie, H. Liu, L.-M. Zhu, H. Li, R. Ran, A free radical assisted strategy for preparing functionalized carbon nanotubes as a highly efficient nucleating agent for poly(l-lactide), RSC Adv. 5(21) (2015) 16604-16610.
[60] V.S.G. Silverajah, N.A. Ibrahim, W.M.Z.W. Yunus, H.A. Hassan, C.B. Woei, A Comparative Study on the Mechanical, Thermal and Morphological Characterization of Poly(lactic acid)/Epoxidized Palm Oil Blend, Int. J. Mol. Sci. 13(5) (2012) 5878.
[61] M. Kaseem, K. Hamad, F. Deri, Y.G. Ko, A review on recent researches on polylactic acid/carbon nanotube composites, Polym. Bull. (2016) 1-17.
[62] B.W. Chieng, N.A. Ibrahim, W.M.Z. Wan Yunus, M.Z. Hussein, Y.Y. Loo, Effect of graphene nanoplatelets as nanofiller in plasticized poly(lactic acid) nanocomposites, J. Therm. Anal. Calorim. 118(3) (2014) 1551-1559.
[63] M. Moniruzzaman, K.I. Winey, Polymer Nanocomposites Containing Carbon Nanotubes, Macromolecules 39(16) (2006) 5194-5205.
[64] N.K. Shrivastava, B.B. Khatua, Development of electrical conductivity with minimum possible percolation threshold in multi-wall carbon nanotube/polystyrene composites, Carbon 49(13) (2011) 4571-4579.
[65] P. Salice, C. Sartorio, A. Burlini, R. Improta, B. Pignataro, E. Menna, On the trade-off between processability and opto-electronic properties of single wall carbon nanotube derivatives in thin film heterojunctions, J. Mater. Chem. C 3(2) (2015) 303-312.
[66] J.J. Xue, J.W. Xie, W.Y. Liu, Y.N. Xia, Electrospun Nanofibers: New Concepts, Materials, and Applications, Acc. Chem. Res. 50(8) (2017) 1976-1987.
[67] A.P. Kishan, E.M. Cosgriff-Hernandez, Recent advancements in electrospinning design for tissue engineering applications: A review, J. Biomed. Mater. Res. Part A 105(10) (2017) 2892-2905.

Highlights:

Nanocomposites were obtained based on carbon nanostructures and poly-L-lactic acid

Functionalized graphene, carbon nanotubes and nanohorns are compared as fillers

Composite electrospun nanofibers have also been prepared

Scanning probe techniques highlight electrical properties of nanofibers

Proven biocompatibility fosters future neuronal tissue engineering investigations